

**NATuRal instability of semiConductors thIn SOLid films for sensing and photonic applications** [Horizon 2020](#)

Project title: **NATuRal instability of semiConductors thIn SOLid films for sensing and photonic applications (NARCISO)**

Grant Agreement: 828890

Call identifier: H2020-FETOPEN-2018-2020/H2020-FETOPEN-2018-2019-2020-01

Start Date of Project: 01/03/2019

Duration: 42 months

Deliverable D3.3– V1.0**Title: Assessment of optical control of MOx wafers**

Leader partner	UNIFI
Author(s)	Francesca Intonti, Marco Abbarchi
Estimated delivery	30/07/2021
Actual delivery	
Revised version	
Work Package	WP3- Nanoimprinting of hierarchically structured surfaces
Tasks	3.3
Dissemination level	Public
Version	1.0

Disclaimer

The content of this deliverable does not reflect the official opinion of the European Union. Responsibility for the information and views expressed herein lies entirely with the author(s).



Contents

Contents	2
1. Introduction	3
2. Characterization of the optical constant and its control	3
3. Quasi-guided modes of titania-based structures obtained via nano-imprint lithography on glass substrates	6
3.1 FDTD calculation of normal reflection and transmission measurements	6
3.2 Normal Reflection and Transmission Measurements	6
3.3 QGMs in TiO ₂ Arrays with a Residual TiO ₂ Layer	9
3.4 QGM Dependance on the Lattice Constants	9
3.5 QGMs Dependance on the Substrate and Residual Layer Properties	10
3.6 Bare Arrays	11
3.7 Optical Properties of the Arrays After the Addition R6G	13
3.8 Confirmation of QGMs by FDTD	15
4. Dark-field spectroscopy	17



1. Introduction

We report on the spectroscopic characterization of metal oxides-based structures deposited via sol-gel dip- (or spin-) coating and printed via nano-imprint lithography. We first provide a characterization of the optical constants of flat, 2D layers via ellipsometry porosimetry showing the control over the refractive index by porosity tuning (see also deliverable D3.2 for a description of the method in use). Thus, we describe the optical properties of printed structures framed in square arrays of nanometric pillars (typical size and pitch ~ 100 nm). This characterization is composed of two parts: 1) the first assessing the average properties of light reflection and transmission under excitation by white light at normal incidence and sampling a large amount of pillars (~ 1 mm spot); 2) the second one instead, by high lateral resolution (~ 1 μm), dark-field spectroscopy at ~ 45 degrees incidence, while scanning the sample to assess its fine features and disorder. In both cases we can highlight the presence of a rather thick residual layer underneath the pillars and thus the onset of quasi-guided modes featuring a high quality factor.

2. Characterization of the optical constant and its control

A characterization of the 2D flat layers was performed in order to determine their properties in terms of refractive index, porosity and roughness. This is done by Environmental Ellipsometry Porosimetry (Figure 1 and 2). The measurements were carried out with a Wollam M200V ellipsometer (350nm-1000nm) measuring in real time the changes of refractive index of a metal oxide thin layer kept in a chamber with controlled atmosphere where air and water were progressively mixed. We thus measured the refractive index evolution upon adsorption/desorption of water, from which isotherms can be extracted and used to obtain the mesoporosity of the layers (pore volume, pore size distribution, pore interconnection through adapted Kelvin models [Loizillon, J. et al., *J. Phys. Chem. C* **2019**, *123* (38), 23464–23479; Boissiere, C. et al., *Langmuir* **2005**, *21* (26), 12362–12371.]).

In the case of porous layers (Figure 1 a and d, respectively for porous TiO_2 and porous SiO_2), when the relative solvent pressure increases, adsorption and capillary condensation occur in the pores. The corresponding adsorbed volume fraction of adsorbate is then deduced from the Bruggeman Effective Medium Approximation [Loizillon, J. et al., *J. Phys. Chem. C* **2019**, *123* (38), 23464–23479] (Figure 1 b and e, respectively for porous TiO_2 and porous SiO_2). The pore size distribution is determined from the isotherm via a modified Kelvin equation to consider the non-spherical geometry of the pores and the thickness of the water layer adsorbed in the pores before capillary condensation (Figure 1 c and f, respectively for porous TiO_2 and porous SiO_2). It can be extracted for nanoporous films (up to pores of ~ 50 nm in diameter).

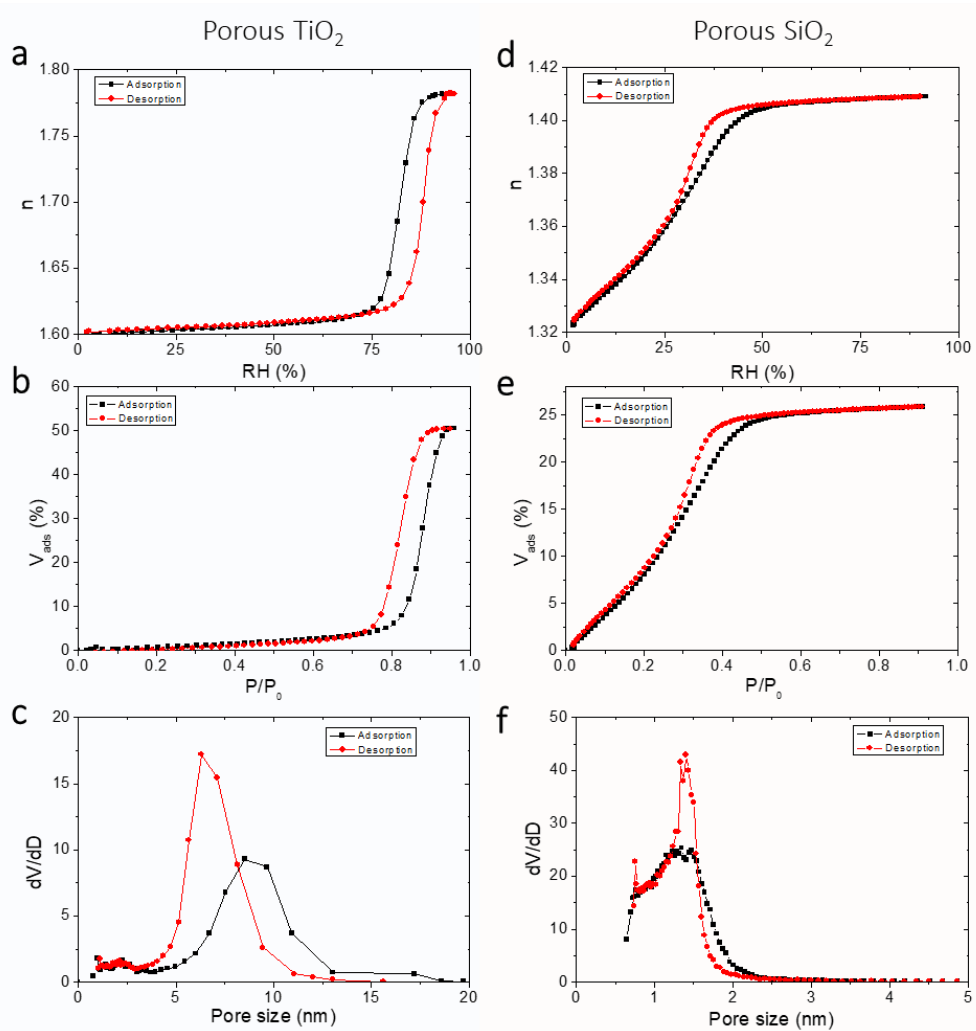


Figure 1. Adsorption/desorption isotherms obtained by ellipsometry porosimetry on a porous TiO_2 layer, 100 nm thick on silicon and on a porous SiO_2 layer, 174 nm thick on silicon. **(a)** Evolution of the refractive index n of a porous TiO_2 layer a function of the relative humidity (RH%) in the atmosphere. **(b)** Adsorbed water volume (%) as a function of the water vapor partial pressure for a porous TiO_2 layer. **(c)** Pore size distribution deduced from the adsorption (black) and desorption (red) curves for a porous TiO_2 layer. **(d)** Evolution of the refractive index n of a porous SiO_2 layer a function of the relative humidity (RH%) in the atmosphere. **(e)** Adsorbed water volume (%) as a function of the water vapor partial pressure for a porous SiO_2 layer. **(f)** Pore size distribution deduced from the adsorption (black) and desorption (red) curves for a porous SiO_2 layer.

Note that the adsorption and desorption curves do not coincide owing to a well-known pore-blocking effect induced by interconnections between pores smaller than the pores themselves (bottleneck pores). Thus, the desorption branch is associated with the interconnections and only the adsorption branch can be exploited to estimate the pore size (even if it occurs out of equilibrium, leading to an overestimation of their dimension). As a first approximation, the adsorption curve provides the size of the smallest dimension of the pores, while the desorption curve provides the size of the interconnections (pore blocking effect).

In the case of thin, porous TiO₂ layers (Figure 1 a, b and c) pore and connections size are of the order of 9 nm and 6 nm respectively with an overall porosity of about 50% determining $n \sim 1.6$. Thus, the case presented here is representative of a rather porous titania layer with a low refractive index. For the thin, porous SiO₂ layer (Figure 2 c, d and e) the porosity is about 25% of the total volume, the pore diameter and connections are below 1-2 nm. The corresponding refractive index is about 1.32, thus smaller than the typical value of 1.5 found for dense silica.

A second example of metal oxides layers is provided for dense materials (Figure 2). In these cases, adsorption/desorption isotherms obtained by ellipsometry porosimetry do not provide a precise estimation of the pore size distribution owing to the low variation of refractive index and low pressure at which the pores load with water, preventing the use of Kelvin's law for capillary condensation. However, a measured refractive index of ~ 2.34 for dense TiO₂ allows to roughly estimate the layer porosity in 10-15% (Figure 3 a). For dense SiO₂ instead the measured refractive index is about 1.43, suggesting a porosity $< 10\%$ vol (Figure 3 b).

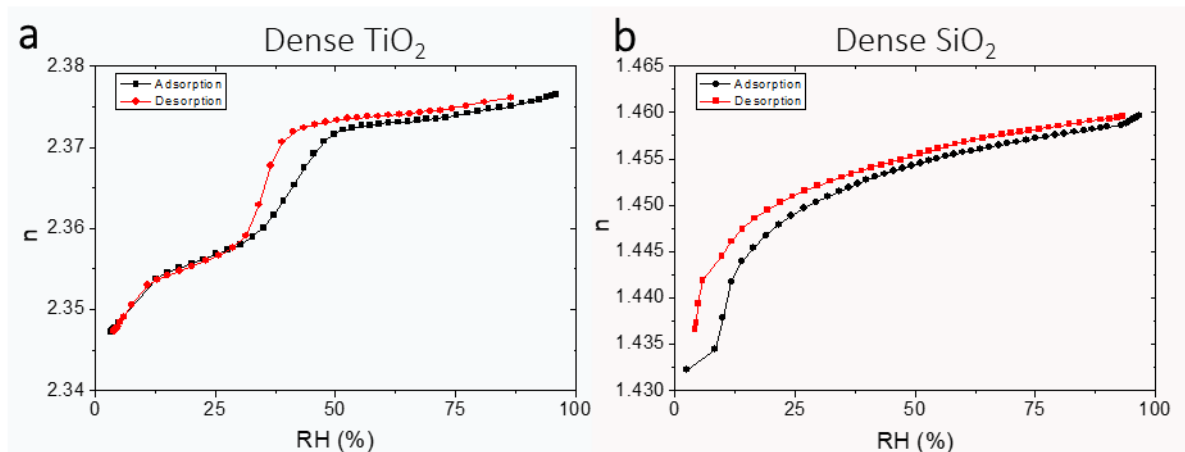


Figure 2. Adsorption/desorption isotherms obtained by ellipsometry porosimetry **(a)** for a dense TiO₂ layer, 62 nm thick on silicon and **(b)** for a dense SiO₂ layer, 137 nm thick on silicon.

Further examples of titania layers with different pore size distributions ($D \sim 2-3$ nm) can be found in references [Bottein, T. et al, *Adv. Funct. Mater.* **2017**, 27 (2), 1604924; Checucci, S. et al., *Advanced Optical Materials* **2019**, 7 (10), 1801406]. For applications in optics, the possibility to adjust the porosity of the sol-gel layers provides a fine tuning of the optical constant of the thin layers and 3D printed structures. It is thus a powerful tool to adjust n to a desired value (e.g. for anti-reflection coatings [Bochet-Modaresialam, M. et al, *ACS Appl. Nano Mater.* **2020**, 3 (6), 5231–5239] and Bragg mirrors).

As for the case of titania, other examples of silica layers featuring a different porosity can be found in [Checucci, S. et al., *Advanced Optical Materials* **2019**, 7 (10), 1801406]. In this latter case, an average pore size of about 7 nm is found with a porosity of 37% determining a refractive index of 1.28. More generally, a plethora of combinations of porosity, pore size distribution, interconnections between pores can be created at will, providing a full control over the micro- and meso-porosity of metal oxides and of their refractive index from low (~ 1.1 for porous MgF₂ [Grosso,



D. et al., *Nature Mater* **2007**, 6 (8), 572–575]) to high (~2.4 for dense titania). This is for instance possible by playing with the initial concentration of templating agents (e.g. cetyltrimethylammonium tetrachloride, Pluronic F127, and poly(butadiene-b-ethyleneoxide).

3. Quasi-guided modes of titania-based structures obtained via nano-imprint lithography on glass substrates

This work reports on TiO₂ arrays fabricated via soft nano-imprint lithography according to the method described in references [Bottein, T. et al, *Adv. Funct. Mater.* **2017**, 27 (2), 1604924; Checcucci, S. et al., *Advanced Optical Materials* **2019**, 7 (10), 1801406]. This work was performed in by an external collaborator (under the guidance of Louise Bradley, School of Physics and CRANN, Trinity College Dublin, Dublin 2, Ireland). A paper on this topic is under review on *ACS Applied Material and Interfaces*.

3.1 FDTD calculation of normal reflection and transmission measurements

To calculate the experimental reflection and transmission spectra from FDTD simulation, one must consider the back reflections from the glass substrate ($n=1.5$), namely of 4%, and the collection angle of the experimental set-up. 0-order reflection and transmission were obtained. Two simulations are needed: one simulation where the incoming beam comes from the air side of the array and another from the substrate side. Simulations do not account for the back reflection of the substrate since the substrate is considered as infinitely thick. From the simulation from the air side, one can obtain the 0-order reflection R and transmission T . From the simulation from the substrate side, one obtains the 0-order reflection R^* and transmission T^* . From these, the total reflection R_T and the total transmission T_T are calculated using:

$$R_T = R + 0.04T^* \quad (4)$$

$$T_T = 0.96T(1 + 0.04R^*) \quad (5)$$

3.2 Normal Reflection and Transmission Measurements

A custom-built experimental set-up was used for the normal incidence and collection reflection and transmission measurements. This set-up allows for collection of light reflected and transmitted from a sample area of $\sim 200 \mu\text{m}^2$. A Xenon lamp was used as an illumination source, a very good collimated white light beam for the length of the set-up was formed. A 50:50 beam splitter (BS) was used to direct the collimated white light beam toward the sample and to allow the collection of the reflected light. The reflection and transmission segments are mirror images of each other, and both use the optics in the same manner. Light from the sample is collected by a 15 cm focal length 2.54 cm diameter lens placed 15 cm away from the sample. An iris with a 0.5 cm opening is placed 12.5 cm away from the sample to reduce the collection angle, this yields a collection angle of 1.2° . A series of lenses are then used to form a magnified image onto an iris where a collection area can be selected by moving the sample stage. The light then into a fibre via a fibre coupler directing the transmitted light into an Andor 230i spectrometer with an Andor CCD camera.



To obtain the percent of transmitted and reflected light through the sample a reference measurement is taken. To obtain the percent of the total light reflected, firstly all spectra collected have the dark spectrum subtracted. The dark spectrum is the background light collected when the white light beam blocked. The reflected light from the arrays was normalized to the reflection of a clean microscope glass slide, then multiplied by the reflection of glass at normal incidence which is approximately 8% accounting for both sides of the glass slide. To obtain the percent of transmitted light through the array, the reflected light was normalized to the transmission when no sample was present.

The particles of these arrays are nanopillars and have Mie resonances in the visible range. The square 2D arrays have an area of 1 mm^2 and vary in nanopillar dimension and periodicity. The periodicity of the arrays allows for surface lattice resonances (SLRs) to exist [V. G. Kravets et al., *Chemical reviews* **2018**, *118*, 5912]; however, for nanoparticle arrays that are constructed on a glass substrate SLRs would not be able to propagate due to the index mismatch between the super substrate (air). Due to the fabrication process of soft nano-imprint lithography, a residual TiO_2 layer is sandwiched between the pillars and the glass substrate, creating the potential for the propagation of quasi-guided modes (QGMs). The novel and advantageous fast large area production for these arrays, and the fact that they can support QGMs without any other fabrication steps, makes them an interesting structure to study as they can be suitable for many applications. Herein we report on the optical properties of the arrays and the conditions under which QGMs can exist.

Three TiO_2 arrays are investigated in this work, and are labelled A600, A550, and A480. These are fabricated together on the same glass substrate but differ from each other by periodicity and pillar dimensions. Scanning electron microscope (SEM) images of the arrays are shown in **Figure 3**. The dimensions of the arrays measured using SEM imaging of focused-ion beam cuts of the sample are given in **Table 1**. In **Figure 3 g-i**, the thickness of the residual layer is measured to be approximately 130 nm. The TiO_2 of the residual layer appears to be more porous and rougher than that composing the pillars. These latter features can be ascribed to relaxation of strain via formation of dislocations after nano-imprint, during the calcination step when the metal-oxide is annealed in order to remove the solvents. The wavelengths the Rayleigh Anomalies (RAs) for rectangular arrays at normal incidence are calculated by the following equation [J. M. McMahon, et al., *Optics express* **2007**, *15*, 18119]:

Table 1. Dimensions of the three arrays. The uncertainty in these measurements is $\pm 10\%$.

Array	Period [nm]	Base Length [nm]	Top Length [nm]	Residual Layer Thickness [nm]	Height [nm]
A600	600	320	170	~130	260
A550	550	280	150	~130	260
A480	480	185	75	~130	280

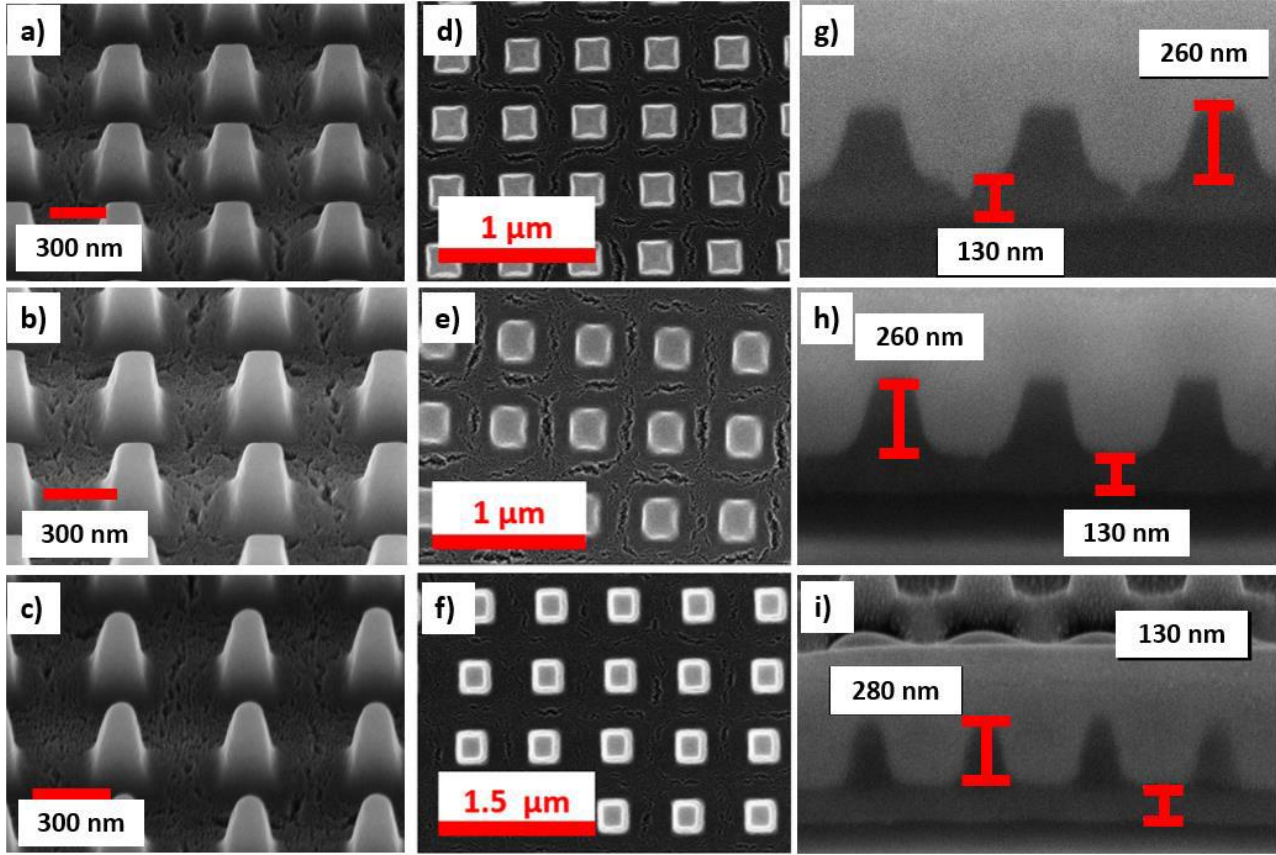


Figure 3. (a-c) Tilted scanning electron microscope (SEM) images of the A600, A550 and A480 arrays, respectively. (d-f) SEM images of the A600, A550 and A480 arrays, respectively. (g-i) SEM images of array cross-sections of the A600, A550 and A480 respectively. The cuts were performed by a focused ion beam.

$$\lambda_{RA} = \frac{n}{\sqrt{\left(\frac{m_x}{a_x}\right)^2 + \left(\frac{m_y}{a_y}\right)^2}} \quad (1)$$

where a_x and a_y are the lattice constants in the x and y direction, m_x and m_y are the positive integers, and n is the refractive index of the environment. Due to the periodicity of these arrays the RAs are in the visible range. The 1st order RA from the air side is denoted as RA (1)_{a,s} = RA (0,1)_{a,s}=RA (1,0)_{a,s} and 1st order RA from the substrate side as RA (1,1)_s = RA (0,1)_s=RA (1,0)_s, the higher order RA will be referred to in a similar manner. The wavelengths corresponding to the RAs are given in **Table 2**.

Table 2. RA wavelengths for the three arrays.

Array	RA(1) _a [nm]	RA(1,1) _a [nm]	RA(1) _s [nm]	RA(1,1) _s [nm]	RA(2) _s [nm]	RA(2,1) _s [nm]
A600	600	424.3	900	636.4	450	402.5
A550	550	388.9	825	583.4	412.5	369.0
A480	480	339.4	720	509.1	360	322.0

3.3 QGMs in TiO₂ Arrays with a Residual TiO₂ Layer

The optical properties of the arrays are also investigated using finite-difference time domain (FDTD) numerical simulations and the conditions under which QGMs can exist in these arrays will be discussed. A schematic of the nanoparticle used in the simulations is shown in Figure 4(a), with the dimensions taken from **Table 1**. The pillars of the array were simulated as truncated round pyramids as seen in the SEM images in **Figure 3**. The radius for the roundness of the pillar is approximately 30 nm. The reflection spectrum is calculated using a normally incident plane wave polarized along the x-axis, Figure 2(b). The glass substrate refractive index is $n = 1.5$, the TiO₂ pillar has a refractive index of 2.1 and the TiO₂ residual layer has an effective refractive index of 1.9. The calculated reflection spectrum for array A550 is shown in **Figure 4(c)**, with the numbers indicating the peak positions.

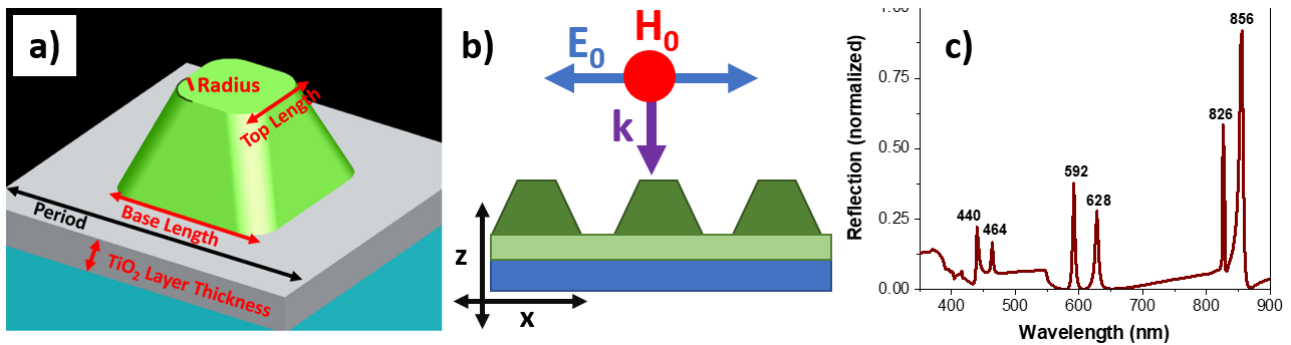


Figure 4. (a) Diagram of geometric array properties used in FDTD simulations, (b) schematic of pillar array with incident plane wave radiation, electric field (with amplitude E_0) and magnetic field (with amplitude H_0), linearly polarized along the x-axis. c) Numerically calculated reflection spectrum for the A550 array with the peak wavelengths given.

The reflection spectrum shows six narrow peaks in pairs, the first pair at 440 and 464 nm, the second pair at 592 and 628 nm and the last pair at 826 and 856 nm. By looking at the magnetic and electric field distribution in the array, it can be immediately seen that for all these peaks, except that at 826 nm, there are high electric and magnetic field intensities in the residual TiO₂ layer. For the peak at 826 nm the field penetrates into the substrate, which could be due to its close proximity to RA(1)_s (see **Table 2** for RA positions for the A550 array). Due to the confinement of the fields in the layer, these peaks are identified as propagating in-plane modes, namely QGMs propagating in the layer. The peaks at 856 and 826 nm are the first order electric and magnetic QGMs and will be referred as E-QGM1 and M-QGM1, respectively. The peaks at 628 and 592 nm are second order electric and magnetic QGMs in the residual layer and they will be referred as E-QGM2 and M-QGM2, respectively. The third set of peaks at 440 and 464 nm are third order electric and magnetic QGMs and will be referred as E-QGM3 and M-QGM3, respectively. In the following sections different parameters of the array will be varied to confirm the behavior of the QGMs with respect to the RAs and the thickness of the layer.

3.4 QGM Dependence on the Lattice Constants

In **Figure 5(a)** one sees the dependence of the reflection spectrum on the lattice constant a_y . One observes that E-QGM1 varies linearly with the change of the lattice constant a_y , while M-QGM1 remains constant. One observes the reciprocal behavior for M-QGM1 and E-QGM1 when the lattice constant in the x direction is varied (not shown). It is clear now that the E-QGM1 is propagating along the y axis and is coupled to the, RA $(0,1)_s$ from the substrate side (825 nm at $a_y=550$ nm) and M-QGM1 is propagating along the x axis and is coupled to RA $(1,0)_s$ from the substrate side (825 nm at $a_y=550$ nm). For the second set of peaks, E-QGM2 and M-QGM2, it is observed that both are varying when either a_x or a_y are varied. Furthermore, their dependence on the lattice constants is not linear, but rather has a $1/\sqrt{c + 1/x^2}$ dependence. Due to the nonlinear dependence on the lattice constant and their proximity to RA $(1,1)_s$ from the substrate, the E-QGM2 and M-QGM2 are clearly coupled with the RA $(1,1)_s$ from the substrate side (583 nm at $a_x=a_y=550$ nm). For the last set of peaks, E-QGM3 and M-QGM3, one observes a very similar behavior to the first set of peaks: E-QGM3 is linearly dependent on a_y while independent of a_x and M-QGM3 is linearly dependent on a_x while independent of a_y . The only RA close to these resonances that would explain this behavior is the second order RA $(2,0)_s$ and RA $(0,2)_s$ (for $a_x, a_y=550$ nm at 412.5 nm). Therefore, E-QGM3 is coupled to RA $(0,2)_s$ and propagating along the y direction and M-QGM3 is coupled to RA $(2,0)_s$ and propagating along the x direction.

3.5 QGMs Dependence on the Substrate and Residual Layer Properties

In **Figure 5(b)**, the dependence of the reflection spectra on the substrate's refractive index is shown. It can be observed that all QGMs positions vary with the refractive index. An asymptotic behaviour is observed for all the QGMs as they approach their coupled RA, further confirming their coupling. In **Figure 5(d)** one sees the impact of the refractive index of the layer on the positions of the QGMs. One can also observe that the index of the layer must be larger than that of the substrates to support QGMs, this is expected as otherwise the layer would not support guided modes. Furthermore, the position of the QGMs can also be tuned by the thickness of the layer (see **Figure 5(c)**). The layer needs to be sufficiently thick to support QGMs, and no lower order QGMs are present for very thin layers. The electric QGMs appear before the magnetic QGMs for each pair when increasing the thickness or refractive index of the layer. The positions of the QGMs are not significantly affected by the pillar's shape and refractive index (not shown). However, the peaks do become broader as the pillars become more optically thick (higher pillar refractive index), as the QGMs are more rapidly scattered out by the pillar.

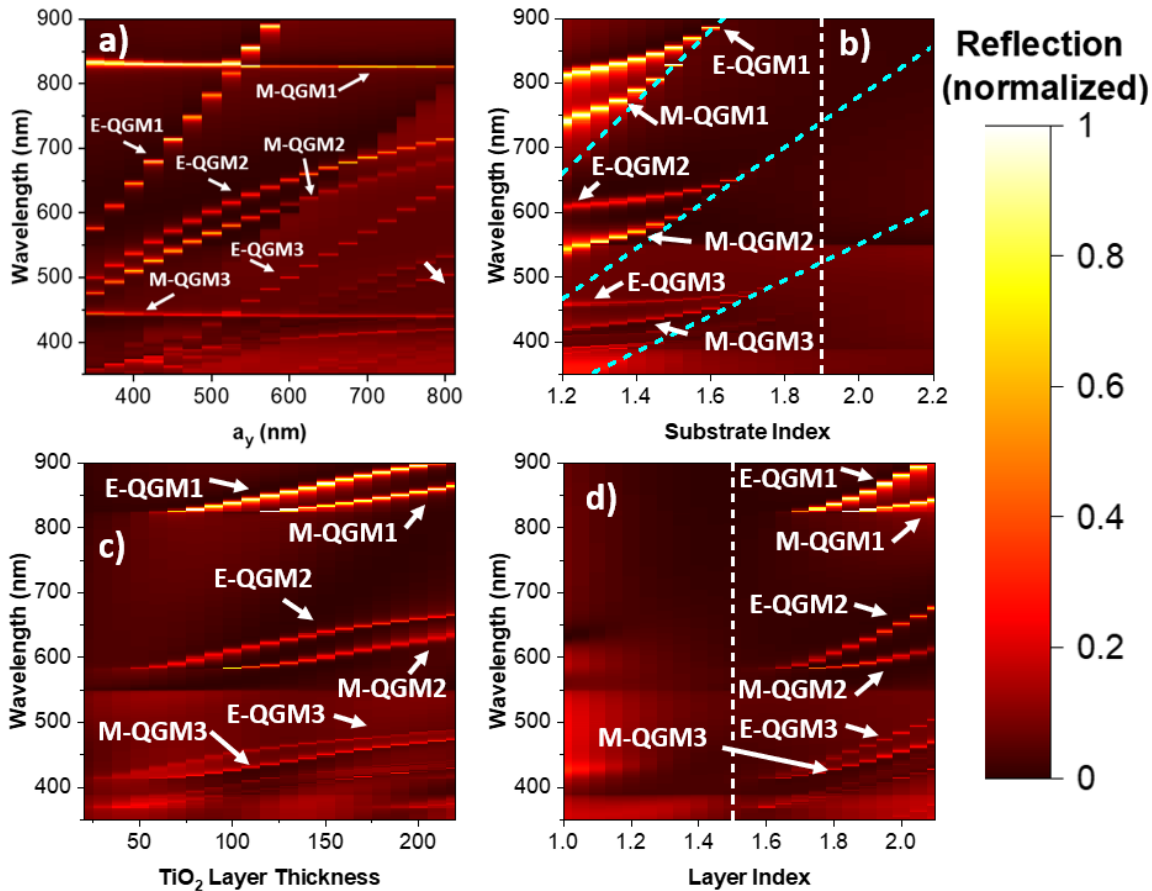


Figure 5. Numerically calculated dependence of the reflection spectrum on a) the lattice constant a_y , b) the substrate refractive index where the blue dashed lines correspond to the RAs and the vertical white dashed line indicates the refractive index of the residual TiO_2 layer, c) the TiO_2 layer thickness and d) the TiO_2 layer refractive index with the vertical white dashed line indicating the refractive index of the substrate.

3.6 Bare Arrays

The experimental reflection and transmission spectra for the three arrays measured under normal incidence illumination are presented in **Figure 6**. The reflection spectra for the three arrays are very similar to each other and in contrast to the numerically simulated spectrum shown in **Figure 4(c)**, no strong sharp peaks are observed. However, features at the RA wavelengths can be seen. At RA $(1)_a$ (see RA positions in **Table 2**), one observes a sharp dip in reflection and at RA $(1,1)_s$, one sees a sudden change in slope for all arrays. For the A550 and A480 at RA $(1)_s$ there is a slight change in slope. One does not observe this feature for the A600 because the RA $(1)_s$ is at 900 nm, which is the limit of the experimental spectral range. For the A600 and A550 near there is again a sharp dip in the reflection spectra. Similar features are observed in the transmission spectra in **Figure 6(b)**, such as at the wavelengths corresponding to RA $(1)_a$ and RA $(2)_s$, and a sudden change in slope in the transmission spectrum at RA $(1,1)_s$. The transmission, reflection or extinction do not show any signs of QGMs coupling to RA. It is attributed to the refractive index of the layer being too low due to the high porosity and increased surface roughness of the TiO_2 layer as seen in **Figure 3(g-i)**.

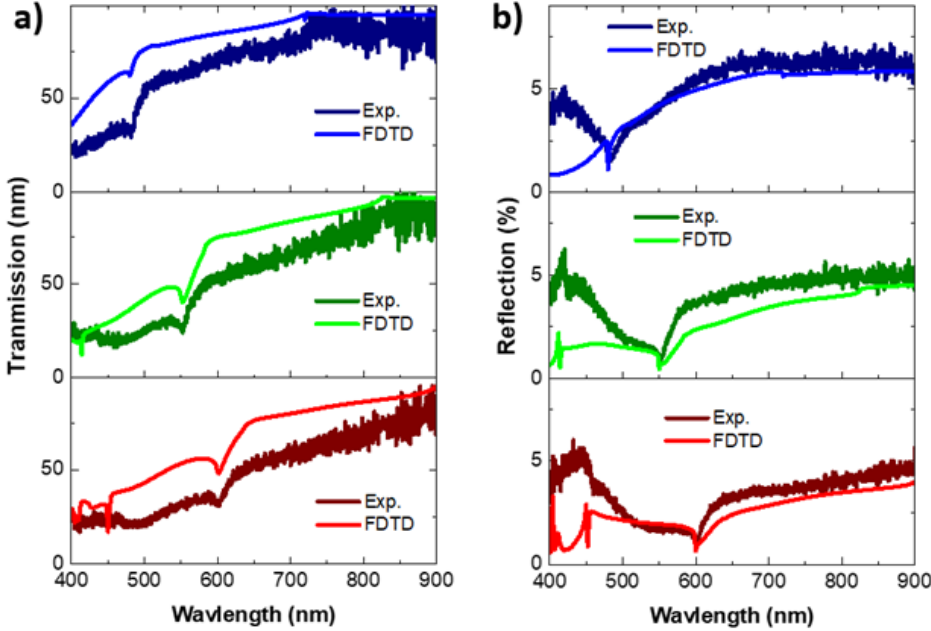


Figure 6. Experimental and FDTD results for the a) normal incidence reflection and b) normal incidence transmission for the A600 (bottom), A550 (middle) and A480 (top) arrays. FDTD simulations consider a 30% porosity for the pillar and 45% porosity for the residual layer with 50 nm root mean square surface roughness.

To further investigate this hypothesis, spectra were simulated using the refractive index of TiO_2 of varying porosity. Experimentally obtained data for the refractive index on a thin TiO_2 layer is used from S. Sarkar, et al., *ACS applied materials & interfaces* **2019**, *11*, 13752.]. The refractive index of TiO_2 for different porosities [P. Karasiński, et al., *Optical Materials* **2016**, *56*, 64] is calculated using the Maxwell-Garnett equation:

$$\frac{n^2-1}{n^2+2} = \left(1 - \frac{P}{100\%}\right) \frac{n_d^2-1}{n_d^2+2} \quad (2)$$

where n is the refractive index, n_d is the refractive index of bulk TiO_2 (roughly 2.54 at 550 nm) and P is the porosity. As commented earlier it can be observed from the SEM images in **Figure 3** that the pillars are smooth and identical to each other, while the layer is not. The surface roughness of the TiO_2 layer is also considered and with the root mean square (RMS) of the surface varied to simulate the randomness of the layer. The impact of randomness in the array on the coupling of RAs with particle resonances has been reported by Zakomirnyi et al *JOSA B* **2019**, *36*, E21.

The randomness in the different features of the array elements (period, size, discontinuities) weakens the collective resonances in the arrays, so one expects to observe similar behaviour for RA-coupled QGMs. The best fit parameters were 30% porosity for the pillar and 45% porosity for the residual TiO_2 layer with 50 nm roughness.

The comparison of the best fit FDTD simulation spectra to the experimental results for the A600, A550 and A480 arrays is shown in **Figure 6**. The shape of the FDTD transmission spectra in **Figure 6(a)** is nearly identical to the experimental transmission for all the arrays. The FDTD transmission is slightly higher than the experimental one, which can arise from imperfections on the backside of the glass substrate and unaccounted effects of the imperfections of the TiO₂ layer and array (e.g. small fluctuations of the sol-gel layer, scattering). The FDTD reflection spectra above 500 nm in **Figure 6(b)** matches well in shape and intensity with the experiments for all the arrays. From 400-500 nm, the FDTD results do not reproduce the increase in intensity observed in the experimental data; this feature is missing in the three arrays. This feature was not reproduced by any combination of refractive index for the pillar and layer. It is possible that it is an artefact from higher order transmission that reflects from the substrate and is detected within the collection angle in the experimental set-up. Provided the presence of cracks in the residual layer, its effective refractive index is lower with respect to that of titania. Thus, it cannot support the propagation of QGMs. However, this porosity provides the possibility to incorporate into the residual layer another material in order to increase its refractive index and recover the conditions for the propagation of QGMs. These features could be in principle, exploited for applications in sensing.

3.7 Optical Properties of the Arrays After the Addition R6G

To investigate the effect of introducing another material four solutions of different concentrations of R6G in ethanol were prepared: 0.25 mM, 0.50 mM, 1.00 mM and 2.00 mM. R6G was added to the arrays by dropping 125 μ L of the solution onto the arrays and let to rest for 30 seconds before spin coating. The arrays were cleaned in acetic acid for 10 minutes, then for 10 minutes with acetone, then rinsed in IPA and dried before spinning on a higher concentration. The effect of the R6G on the optical properties of the array was reversible; after cleaning the sample the reflection and transmission spectra returned to that of the base array. The influence of R6G on the reflection and transmission spectra of the arrays can be seen in **Figure 7**. Very sharp and strong reflection peaks at high R6G concentrations emerge the A550 and A480 arrays. The features of experimental spectra will be discussed first, followed by numerical simulations to confirm the presence of the QGM after the incorporation of R6G dye into the arrays.

The effect of R6G on the A550 array will be looked at first, as it shows the most features. The two lower concentrations (0.25 and 0.50 mM) of R6G on the A550 array yielded virtually no changes in the reflection spectra (**Figure 7**). For the higher concentrations, one can observe a very strong reflection peak at 835 nm very near RA(1)_s at 825 nm. This peak is likely to result from an electric QGM coupled RA(1)_s (E-QGM1). The sharp peaks at 594 and 626 nm are not nearly as strong in reflection as the E-QGM1 peak, i.e. less than 10%. In the simulation they are usually approximately half of the intensity of the E-QGM1, as seen in Figure 4. From the Fano-shape of these peaks and their close position to the RA(1,1)_s, these are attributed to the electric and magnetic QGM coupled RA(1,1)_s i.e. E-QGM2, M-QGM2, with E-QGM2 at 626 nm and M-QGM2 at 594 nm. The RA(1)_a feature at 550 nm is present for all concentrations and does not change in position. This correlates to the R6G being present mostly in the layer and possibly forming a thin layer on top. If the layer is too thick, the RA(1)_a is lost and a new RA(1) related to the refractive index for the thick layer would appear. One can also observe how the small feature related to RA(2)_s become slightly more



prominent and how it redshifts. The redshift is caused mainly by an increasing refractive index in the layer but can also occur by increasing the layer thickness. Significant changes in transmission are also observed at the higher concentrations of 1.00 mM and 2.00 mM. For 2.00 mM, there is a dip in transmission at 628 nm and at 835 nm corresponding to the E-QGM2 and E-QGM1 peaks observed in reflection, respectively. Lastly, the reflection and transmission in the region between 450-550 nm is lower due to the absorption of the R6G (not shown). For the 1.00 mM, the transmission spectrum does not correspond well with the reflection spectrum owing to the uneven spread of R6G (not shown). Despite this, the spectrum is interesting as it shows that the region measured has a slightly lower concentration of R6G, resulting in a layer with lower refractive index; the E-QGM2 dip blueshifts and, similarly, the dip at E-QGM1 is not nearly as strong and is blue shifted to the RA.

Similar observations are made for the effects of R6G on the reflection of the A480 array. Again, no QGMs were observed for the lower concentrations. However for the 1.00 mM concentration, one observes a sharp peak in reflection at 736 nm, attributed to an electric QGM coupled to $RA(1)_s$ (E-QGM1). No QGM coupled to the $RA(1,1)_s$ are observed since the $RA(1,1)_s$ is at 509 nm. This is expected, as 509 nm is in a region of high R6G absorption preventing the formation of a QGMs. At 2.00 mM, one can observe how the spectra looks like before being able to support E-QGM1, as the R6G concentration is not as high to prevent its formation. In the transmission spectra one notices two dips at 730 nm and 757 nm, these are attributed to the M-QGM1 and E-QGM1, respectively, as the magnetic QGM occurs at shorter wavelengths than the electric QGM and because of their proximity to $RA(1)_s$ and sharp Fano lineshape. One can also appreciate the increased concentration of R6G on the A480 array at 1.00 mM from the dip in transmission between 500-550 nm, which is a direct consequence of high R6G concentrations. For the A600 array the experimental spectral range does not expand to wavelengths higher than 900 nm, therefore QGMs coupled to $RA(1)_s$ are not detectable. For 1.00 mM, there is a peak at 647 nm, which is quite close to the RA at 636 nm and attributed to the E-QGM2. The refractive index of the layer is not high enough to support M-QGM2. For the same reasons as in the previous arrays, one does not observe any QGMs coupled to $RA(2)_s$. None of the other concentrations show any QGMs. The transmission spectra for the A600 at 1.00 mM does not quite match with the reflection following the trend of the previous arrays at this concentration due to the uneven dye distribution. Based on the plateau observed around 650 nm at this concentration, the A600 array might be supporting E-QGM2 and M-QGM2, however it is not conclusive.

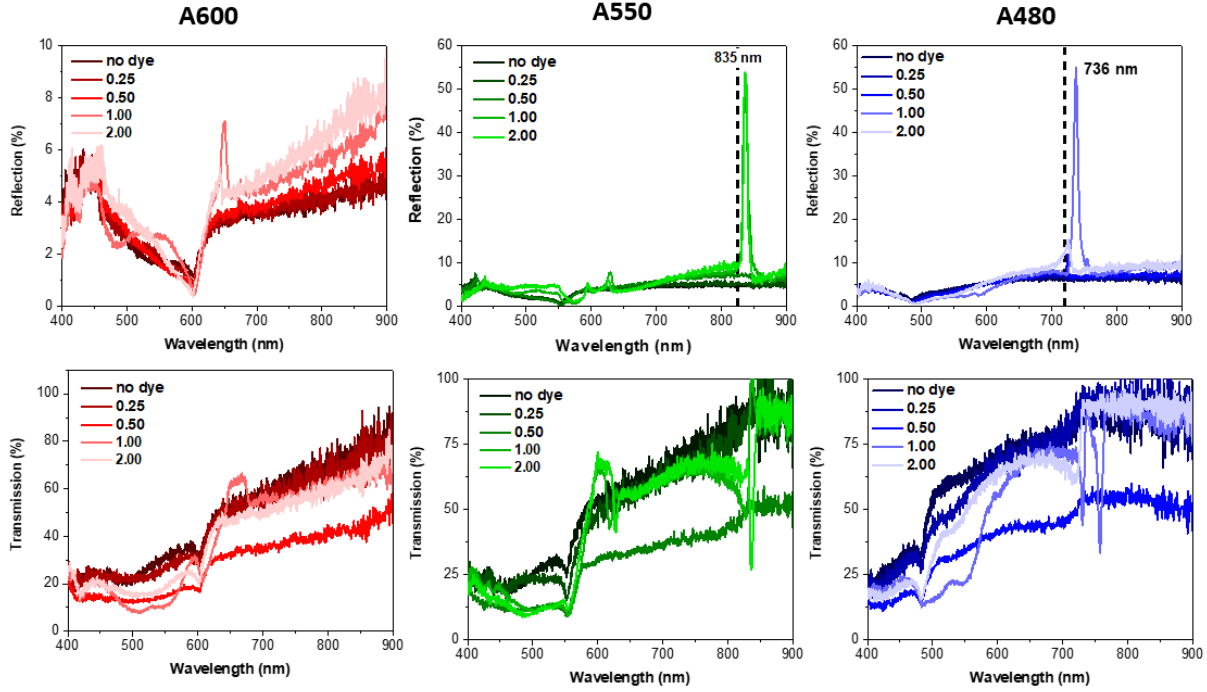


Figure 7 Dependence of the experimental reflection (top row) and transmission (bottom row) on increasing R6G concentration on the A600, A550 and A480 arrays. The black dashed line shows the position of RA(1).

3.8 Confirmation of QGMs by FDTD

The relation of these peaks to the QGMs will be verified by FDTD simulations. We showed that the QGMs are most strongly influenced by the properties of the layer and the substrate. To investigate the effect of the R6G it is assumed in the simulation that the R6G is only affecting the layer, it penetrates the layer uniformly and the layer is flat. The effective refractive index for a mixed layer of R6G and TiO₂ was calculated by using the Maxwell-Garnett equation.

$$\frac{n_{eff}^2 - n_{TiO_2}^2}{n_{eff}^2 + 2n_{TiO_2}^2} = \delta \left(\frac{n_{R6G}^2 - n_{TiO_2}^2}{n_{R6G}^2 + 2n_{TiO_2}^2} \right) \quad (3)$$

where n_{eff}^2 is the effective refractive index, n_{R6G}^2 is the refractive index of R6G, $n_{TiO_2}^2$ is the refractive index of TiO₂ and δ is the volume fraction of R6G. Since the concentration of R6G and porosity of TiO₂ in the residual layer and R6G concentration are unknown, different combinations of TiO₂ porosity and R6G are tested. The 100% and 60% l.p. cases provide good agreement of the spectral shape with the measured reflection and transmission spectra of the A550 for R6G concentrations of 2.00 mM, **Figures 8(g)** and **8(h)** respectively. The peak positions in FDTD reflection spectrum are a slightly better match for the 60% l.p. refractive index. It is noted that the peak at 626 nm is larger than in the experimental spectrum. This could be due to a higher concentration of R6G being present or due to the tail of the R6G absorption on the arrays being slightly longer due to formation of j-aggregates on the arrays. The peak of the j-aggregate absorption is roughly at 550 nm^[50]. The features of the sharp dips in the transmission spectra shown in **Figure 8(h)** also agree



well with the experimental results and the overall spectral shape matches very well with the experimental results, except in the region between 450-550 nm. The shape of this region in experiment is mainly caused by the absorption of R6G in this region. The 100% R6G concentration layer matches with this section better as it has a higher R6G concentration than the 60% l.p layer. These relative ratios of TiO_2 to R6G give the good correspondence with the experimental data and can reproduce all the main spectral features, however, it is also possible to obtain similar agreement using a higher concentration of R6G and different porosity ratios.

One can confirm that the sharp peaks observed in reflection in the FDTD simulations are QGMs by comparing the field maps for the array with a layer 60% l.p and those for the TiO_2 arrays with no porosity. The electric and magnetic field intensity distributions for the M-QGM2 at 594 nm are shown in **Figures 8(a) and 8(b)**, respectively. The electric field forms a loop around the layer and substrate, which confirms that this is a magnetic QGM traveling along the y axis. The three lobes of the magnetic field in the layer indicate that this is a M-QGM coupled to $\text{RA}(1,1)_s$. Similarly, for the E-QGM2 at 624 nm, the magnetic field forms a loop around the layer in **Figure 8(d)** and there are three intense electric field lobes confined mostly in the layer in **Figure 8(c)**, confirming that this is an electric QGM propagating along the x axis which is coupled to $\text{RA}(1,1)_s$. The electric and magnetic field profiles for the E-QGM1 at 835 nm are shown in **Figure 8(e) and 8(f)**, respectively. A magnetic loop and high electric field intensity in the layer show that this is an electric QGM traveling in the y direction which is coupled to $\text{RA}(1)_s$. The simulations confirm that the sharp reflection peaks and transmission dips observed with the addition of R6G in the experiments are directly related to QGMs coupled to RAs. However, no higher order QGMs are observed for $\text{RA}(2)_s$ due to high losses from the R6G absorption in the layer in the range from 400-580 nm.

Thus, it is demonstrated that absence of the QGMs arises from the porosity and roughness of the residual TiO_2 layer, which lowers its effective refractive index. The porosity and roughness can also be of benefit as the properties of the layer can be easily tuned by incorporating different materials to increase the effective refractive index. It is demonstrated that QGMs can be observed by the incorporation of R6G onto the arrays. First and second order electric and magnetic QGMs are observed at high R6G concentrations. The presence of QGMs was verified by inspection of the calculated electric and magnetic fields maps. Furthermore, this process is reversible. The residual layer, which is a consequence of the soft-NIL fabrication process, has a significant effect on the optical properties of the TiO_2 arrays. It can be used to manipulate the optical modes of the array and can potentially be exploited in sensing applications.

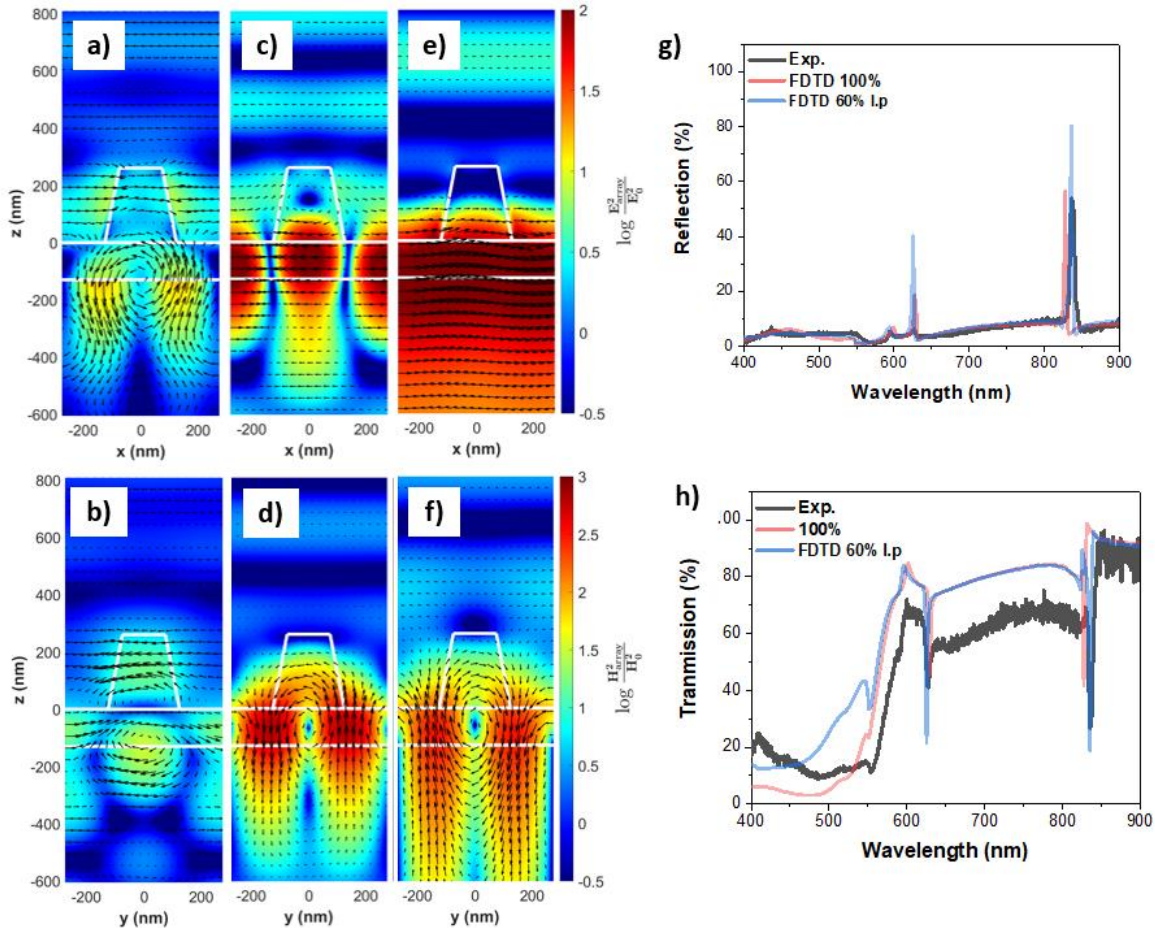


Figure 8. Electric and Magnetic field intensity distributions normalized to the incident field intensity for the A550 array with R6G incorporated into the residual TiO₂ layer (60% l.p). The colour represents the intensity on a logarithmic scale and the black arrows represent the real part of the vectorial electric/magnetic field on the xz/yz plane. a) shows the electric field intensity distribution and b) magnetic field intensity distribution for M-QGM2 at 594 nm. c) shows the electric field intensity distribution and d) magnetic field distribution for E-QGM2 at 628 nm. e) shows the electric field intensity distribution and f) magnetic field intensity distribution for E-QGM1 at 835 nm. Experimental spectra for the arrays with R6G concentration of 2.00 mM and FDTD simulation spectra for different TiO₂/R6G ratios: g) reflection and h) transmission.

4. Dark-field spectroscopy

A set of samples, replica of the bare arrays discussed above, has been also investigated by dark-field spectroscopy at UNIFI. The custom-built experimental set-up (sketched in **Figure 9**) was implemented on a commercial Scanning Near Field Optical Microscope (TwinSNOM by Omicron), which in turn was already assembled on an optical Zeiss microscope conveniently modified to house the near field tip holder together with scanning stages. A great advantage of this set-up is that, exploiting the piezoelectric stages (P-500 by Physik Instrumente), is possible to perform scanning dark-field optical maps, in which at each pixel of the map corresponds a single acquired spectrum.

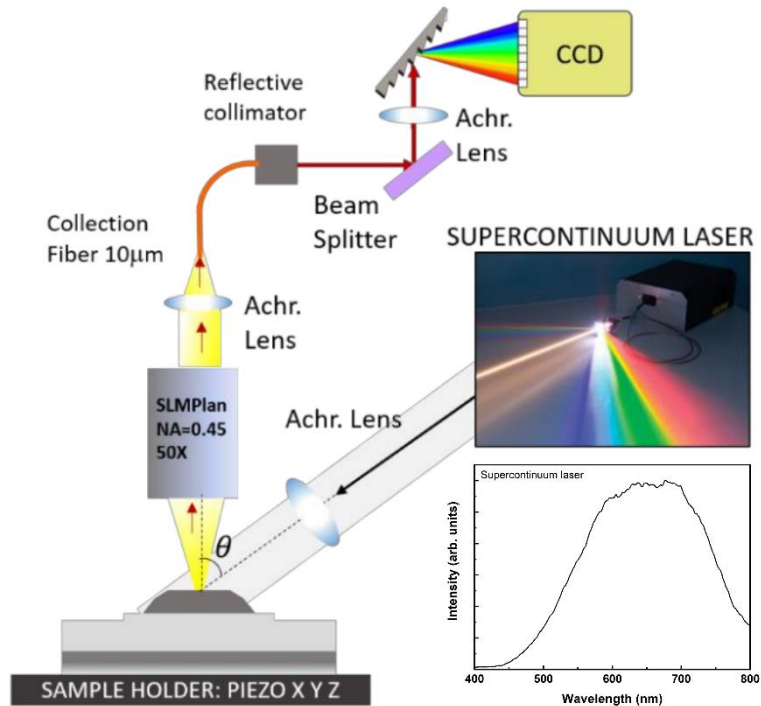


Figure 9. Schematic representation of the dark-field spectroscopy set-up.

To achieve the dark-field regime, a supercontinuum laser (Leukos-STM) whose emission spectrum is reported in fig. 1c, ranging mainly in the wavelength interval (500-800) nm, is focalized with an achromatic lens of 6 cm focal length on the sample surface. The supercontinuum laser beam is tilted by an angle $\theta=50^\circ$ with respect to axis normal to the sample, larger than the collection angle (given by the numerical aperture $NA=0.45$ of the objective). This arrangement assures that the objective collects only the light scattered by the sample, which is then focalized on a multimode optical fiber of 10 μm core with an achromatic lens of 3 cm focal length. At the other end of the fiber the scattered signal is extracted with a reflective collimator and then focalized with an achromatic lens of 5 cm focal length on the slit of a spectrometer (equipped with a 150 lines/mm grating that exhibits a 500 nm blaze), where it is dispersed and finally detected by a liquid nitrogen-cooled CCD detector.

The sample investigated was a single glass substrate containing nine arrays of 150 nm wide trenches milled with variable pitch (380, 400, 420, 440, 460, 480, 500, 550, and 600 nm) in a squared geometry. By exploiting the piezoelectric stages, a $10 \times 10 \mu\text{m}^2$ dark-field optical map was acquired in the center of each pad and, being the scanning step equal to 500 nm, 400 spectra were collected for each periodicity of the pillars.

The dark-field optical map acquired on A400 (i.e. where the pitch periodicity is 400 nm) is reported in **Figure 10 a)**; although the periodic structures are not visible (being the periodicity of the pillars smaller than the scan step), one can get important information about the homogeneity of the sample on a relatively large scale. The spectra acquired in different pixels (see **Figure 10 c)-f)**) display very sharp resonances whose spectral position does not shift across the sample. However, since the relative intensity of the peaks fluctuates from pixel to pixel, in **Figure 10 b)** is reported the mean spectrum averaged over the whole dark-field map.

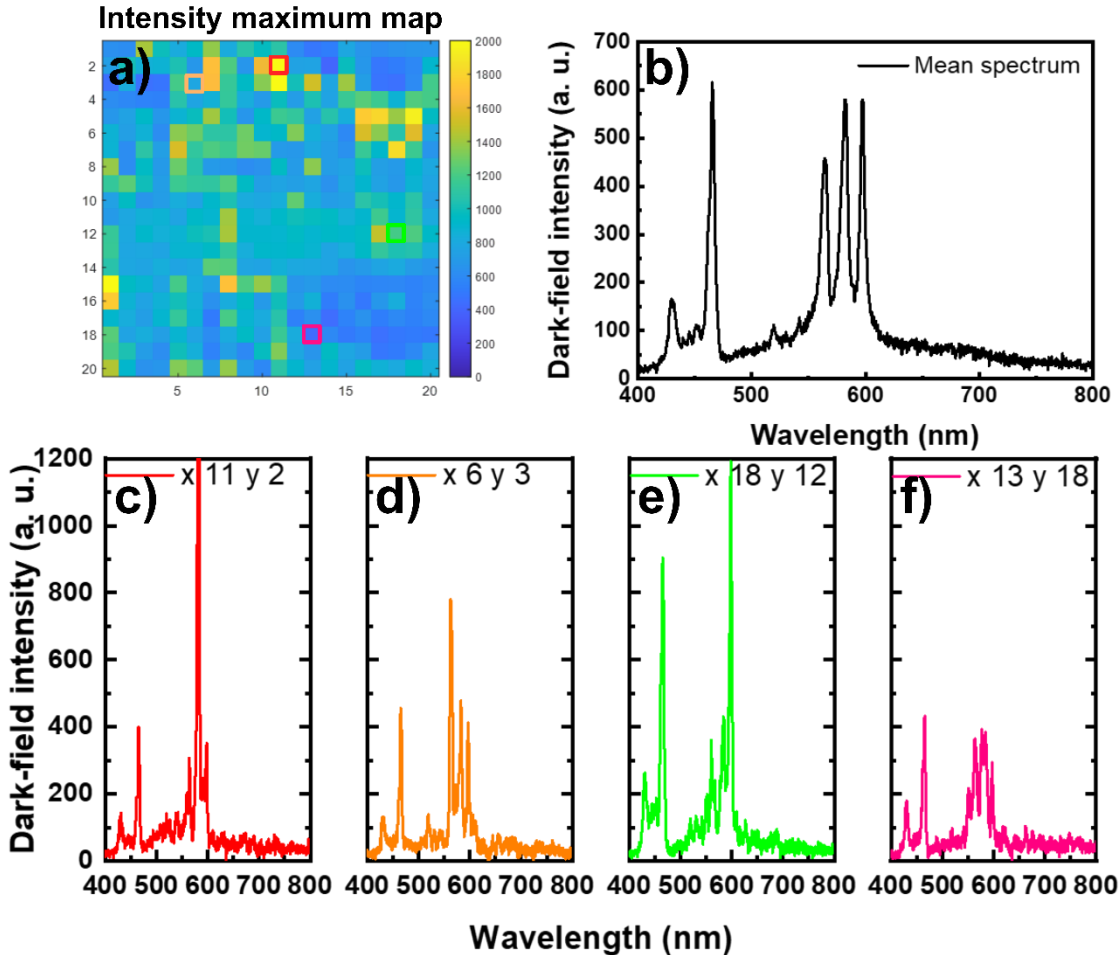


Figure 10. a) Dark-field optical map of A400 with dimension of $10 \times 10 \mu\text{m}^2$ and 500 nm/px steps, acquired in the wavelength range (400-800) nm. b) Mean dark-field spectrum of the map. c)-f) Four spectra relative to different pixels (red, orange, green, magenta).

The mean spectra of the $10 \times 10 \mu\text{m}^2$ dark-field optical maps acquired on the nine different arrays are reported in **Figure 11**. The data show sharp resonances red-shifting and growing in intensity with increasing pitch size. However, the increase of the pitch size is followed by an increase of the width of the resonances, and, in the samples with the larger pillars, the bandwidth is comparable to that of the supercontinuum laser. The broadening of the scattering spectra at increasing size of the pillars could be attributed to the overlap of higher order modes, that are investigated in the following.

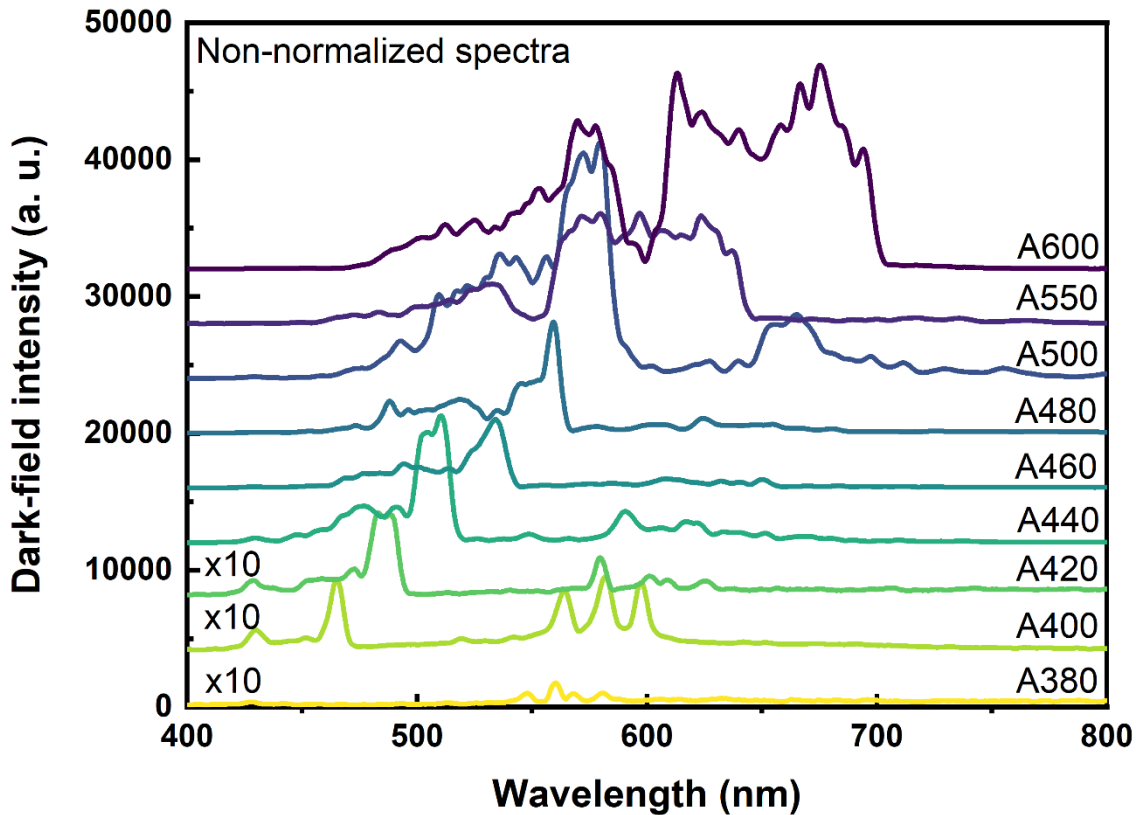


Figure 11. Mean dark-field spectra of $10 \times 10 \mu\text{m}^2$ maps. The spectra for pitch ranging from 380 up to 600 nm are vertically offset for clarity and are not normalized to the supercontinuum laser used for illumination.

To understand the influence of the tilted illumination in respect to what reported in the initial part of this section with normal incidence, we performed FDTD numerical simulation of the A400 array. An infinite glass was used as substrate, while a 130 nm thick layer of TiO_2 ($n=1.9$) was placed atop the substrate. The resonator was modelled as a 280 nm tall pillar with a 250 nm wide side and refractive index 2.1. A rectangular simulation region was used with the z-axis perpendicular to the surface of the substrate and the simulation region extents in the x- and y-directions both equal to the period of the TiO_2 array. Periodic boundary conditions were used for the x-min, x-max, y-min and y-max faces of the boundary, whereas perfectly matched layer boundary conditions were used for the z-min and z-max planes. The incident plane wave was delivered at a 45° angle to the sample surface from the right with a wavelength range from 400 nm to 800 nm. Field monitors were respectively placed in the xy-plane 120 nm above the source and in the xz/yz-planes through the center of the pillar to measure the reflected power and the electric and magnetic fields.

The fraction of the electric field intensity $|E|^2$ integrated over the solid angle given by the numerical aperture of the objective is reported in **Figure 12 a)** showing good agreement with the experimental dark-field spectrum (**Figure 12 b)**), especially for what concerns the sharp resonances.

By looking at the electric and magnetic field intensity distributions of the peaks observed in **Figure 12 a)**, reported in **Figures 12 c)-n)**, we can confirm if the observed resonances are related to QGMs. As an example, the magnetic loop and the high electric field intensity in the TiO_2 layer, observed in **Figure 12 n)** and **m)** respectively, show that the sharp peak at 591 nm is an electric

QGM travelling in the y direction. The only peak that is not related to QGMs is the sharp resonance at 440 nm. From the analysis of the distributions of the electric and magnetic field reported in Figures 12 e) and f), respectively, we attribute this optical feature to a surface lattice resonance (SLR), i.e. an enhancement of the single particle resonance by the in-plane diffraction orders of the lattice [Castellanos, G. et al., J. Appl. Phys. 125, 213105 (2019)].

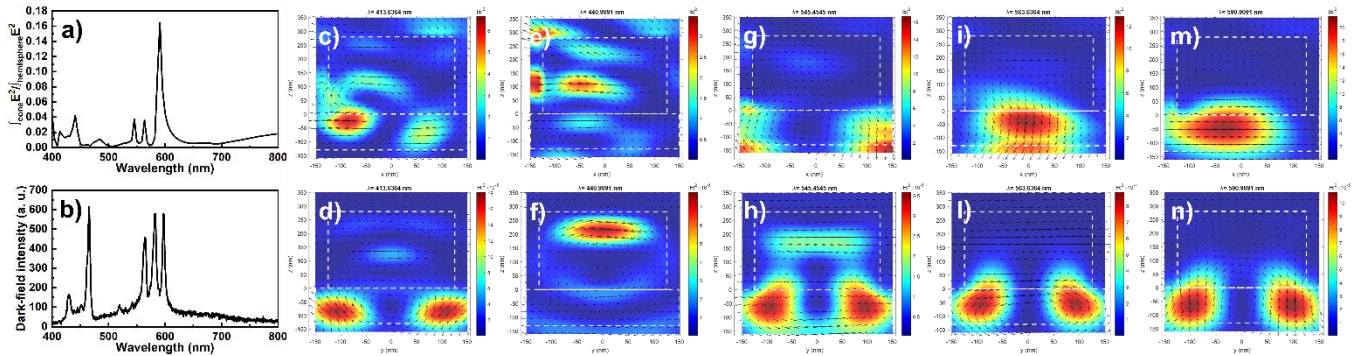


Figure 12. a) Fraction of the electric field intensity $|E|^2$ integrated over the solid angle given by the NA of the objective. b) Experimental dark-field spectrum. c), e), g), i), m) show the electric field intensity distribution and d), f), h), l), n) the magnetic field intensity distribution for the peaks observed in a). The colour represents the intensity and the black arrows represent the real part of the vectorial electric/magnetic field on the xz/yz plane.

In conclusion, by means of the custom-built dark-field spectroscopy set-up at UNIFI, we have confirmed the results obtained by light reflection and transmission by the external collaborators in Dublin. We intend to further investigate the influence of the illumination angle θ on the spectral features of QGMs in order to tune their spectral position not only by changing the pillar dimensions, but also by modifying the illumination condition.

Moreover, the feasibility to perform dark-field maps and thus obtain the spatial distributions corresponding to every wavelength of the dark-field spectrum, is extremely appealing for the investigation of isolated single dewetted islands (materials from WP1) where the spatial periodicity of the resonators is larger than the lateral spatial resolution of the set-up.